Journal of Innovative Technology, Vol. 2, No. 2, pp. 43-46, September 2020
http://doi.org/10.29424/JIT.202009_2(2).0007

Coupling Efficiency of Terahertz Antiresonant Reflecting Hollow Waveguides

Chih-Hsien Lai [1*] and Yueh-Chi Lai [2]

ABSTRACT

We numerically investigate the coupling efficiency, *i.e*., the percentage of coupled power, from the light source to the terahertz antiresonant reflecting hollow waveguides. Numerical results show that the coupling efficiency depends strongly on the operating frequency. To be specific, the coupling efficiency can be well above 90% at most frequencies. However, it drops significantly at the resonant frequencies on account of the mode mismatch between the field distribution of input source and the modal pattern of the waveguide mode. The case where a pipe waveguide is connected to another pipe waveguide of different size is also examined, which is considered important for system integration. It is found that, coupling efficiency between the connected pipe waveguides can be high, but the resonant frequencies should be still avoided for efficient operation.

Keywords: Coupling efficiency, antiresonant reflecting waveguides, hollow waveguides, terahertz waveguides.

1. INTRODUCTION

In order to integrate optical systems, optical waveguides are essential to transmit light from the light source, between the optical devices, and to the optical detector (Schultz 1979; Milvich *et al*. 2018; Chou Chao *et al*. 2019a; Chou Chao *et al*. 2019b; Wang and Dong 2020; Chou Chao *et al*. 2020). When it comes to terahertz (THz) wave, which is usually defined as an electromagnetic band locating between 0.1 to 10 THz, a lot of waveguides have been proposed for THz transmission, including metal waveguides (Han *et al*. 2007), dielectric waveguides (Yang *et al*. 1990), subwavelength fibers (Dupuis *et al*. 2009), porous waveguides (Arrand et al. 1997), photonic crystal fibers (Matsui *et al*. 2009), etc. Among these proposed THz waveguides, the metal waveguides have high skin-depth loss, and the dielectric waveguides suffer strong absorption loss. On the other hand, although the porous waveguides and the photonic crystal fibers have less loss in the THz regime, they are difficult to fabricate.

It is now well known that the dry air is the most suitable medium to transmit THz wave. Based on this finding, THz hollow-core pipe waveguide (Lai *et al*. 2009) was proposed for transmission. It has a large air core and a thin dielectric pipe of low refractive index for cladding. The cladding layer functions like a Fabry-Perot etalon (Duguay *et al*. 1986). It has been shown that as long as the operation frequency is close to the resonant frequencies of the etalon, the cladding layer becomes transparent, and THz waves will leak to the outside of the pipe waveguides. However, at antiresonant frequencies, the cladding layer provides strong reflections so that THz waves can be well confined in the air-core region, and low transmission loss can be successfully achieved (Lai *et al*. 2010).

Manuscript received July 16, 2020; revised August 6, 2020; accepted August 27, 2020.

[1*] Professor (corresponding author), Department of Electronic Engineering, National Yunlin University of Science and Technology, Yunlin, Taiwan 64002, R.O.C. (e-mail: chlai@yuntech.edu.tw).

[2] Master Student, Department of Electronic Engineering, National Yunlin University of Science and Technology, Yunlin, Taiwan 64002, R.O.C.

From an application perspective, having developed the high-performance pipe waveguides for THz transmission, the next important step is to investigate the coupling efficiency of the THz pipe waveguide, *i.e*., to examine by what percentage the power emitted from the THz source can be coupled into the pipe waveguides. In this reported research, this issue is numerically studied. It will be shown later that, for the THz pipe waveguides, the coupling efficiency heavily depends on the operating frequency. Therefore, it is important to select the frequency to have a high coupling efficiency for the applications of the THz pipe waveguides.

2. NUMMERICAL METHOD

This reported research was numerically performed by using a finite-difference frequency-domain (FDFD) method proposed by Yu and Chang (2004). This method provides a full vectorial mode solver, which can figure out the eigenmodes of waveguides. Assuming the waveguide is invariant along the *z*-direction, essentially, the FDFD mode solver is to solve a complex eigenvalue equation as shown below:

$$\mathbf{P}\begin{bmatrix}\mathbf{E}_x\\ \mathbf{E}_y\end{bmatrix}=\begin{bmatrix}\mathbf{P}_{xx} & \mathbf{P}_{xy}\\ \mathbf{P}_{yx} & \mathbf{P}_{yy}\end{bmatrix}\begin{bmatrix}\mathbf{E}_x\\ \mathbf{E}_y\end{bmatrix}=\beta^2\begin{bmatrix}\mathbf{E}_x\\ \mathbf{E}_y\end{bmatrix} \tag{1}$$

where the eigenvalue is the square of the complex propagation constant β, and the eigenvector is the *x*- and *y*-components of the electric field, $\mathbf{E}_x$ and $\mathbf{E}_y$. Attenuation constant α of the waveguide can be obtained from the imaginary part of the complex propagation constant as $\alpha = -2\,\mathrm{Im}(\beta)$.

After solving the electric field distribution of the pipe waveguide, the coupling efficiency of the THz source to the pipe waveguide can be calculated by the following overlap integral equation:

$$\eta=\frac{\left|\iint E_s\cdot E_g^*\,dxdy\right|^2}{\iint\left|E_s\right|^2 dxdy\ \iint\left|E_g\right|^2 dxdy} \tag{2}$$

where E_s is the electric field distribution of the THz source, and E_g is the electric field distribution of the fundamental mode of the waveguide. In this work, we assume the THz source is a Gaussian beam. In other words, the electric field distribution of the input source has the form of exp ($-\frac{x^2+y^2}{w_0^2}$), where $2w_0$ is the width of the beam waist.

3. NUMERICAL RESULTS

Cross-section of the THz pipe waveguides is illustrated in Fig. 1(a), and the parameters used in this work are: core width w = 7 mm, refractive index of core n_1 = 1 (air), thickness of cladding layer t = 1 mm, and refractive index of cladding layer n_2 = 1.4 (Teflon). For the convenience of discussion, we have considered the case of the slab-type antiresonant reflecting hollow waveguide first. As depicted in Fig. 1(b), the slab-type antiresonant reflecting hollow waveguides can be treated as the one-dimensional (1D) version of the two-dimensional (2D) circular pipe waveguides. According to the literature (Lai *et al.* 2010; Lai *et al.* 2011), the transmission spectrum of the antiresonant reflecting hollow waveguide, either the 1D (slab-type) or the 2D (circular-type) version, can be partitioned periodically into several pass-bands. The lowest transmission loss of each band occurs at the antiresonant frequencies as given by

$$f_a = \frac{\left(m-\frac{1}{2}\right)c}{2t\sqrt{n_2^2-n_1^2}}, \quad m = 1, 2, 3, \ldots \tag{3}$$

where c is the velocity of light in free space. Using parameters specified previously and taking m = 2, 3, 4, 5, and 6 into Eq. (3), antiresonant frequencies can be obtained to be 230, 383, 536, 689, and 842 GHz, respectively. Here, we have chosen the operating frequency to be the antiresonant frequency of the forth pass-band (m = 4), *i.e.*, f_a = 536 GHz. Then, we would like to find out the optimal beam waist ($2w_0$) of the input Gaussian beam so that it would have the maximum coupling efficiency under the operating frequency. Calculation using Eq. (2) shows that the optimal beam waist $2w_0$ is 5 mm when the operation frequency is 536 GHz, as shown in Fig. 2(a). Moreover, further calculation indicates that, under the assumed structure parameters, the optimal beam waists are all the same (5 mm) when the operation frequency is chosen to be the antiresonant frequencies of the five pass-bands for which m = 2, 3, 4, 5, and 6, as shown in Fig. 2(b). In the following, we assume that the input Gaussian source has a beam waist of 5 mm.

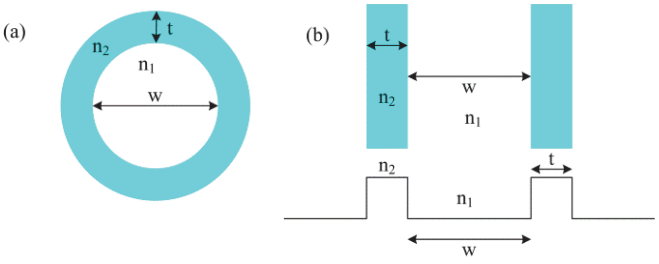

Fig. 1 (a) Cross-section of the THz pipe waveguide. (b) Structure of the slab-type antiresonant reflecting hollow waveguide and the corresponding refractive index distribution.

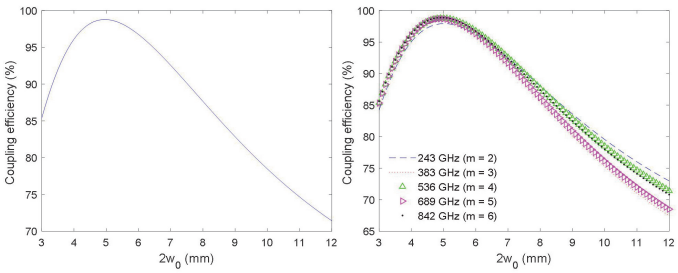

(a) (b)

Fig. 2 Coupling efficiency of the Gaussian beam to the slab-type antiresonant reflecting hollow waveguide as a function of beam waist $2w_0$. (a) The operation frequency is 536 GHz. (b) The operation frequency is 230, 383, 536, 689, and 842 GHz, respectively.

Figure 3(a) plots the attenuation constant of the slab-type antiresonant reflecting hollow waveguide as a function of frequency. As can be seen from Fig. 3(a), there are five pass-bands, which corresponds to m = 2, 3, 4, 5, and 6, respectively. Moreover, the lowest attenuation constant of each pass-band occurs at the antiresonant frequencies as calculated above. However, it is noted that there are some frequencies at which the attenuation constant is especially large. In fact, these frequencies are the resonant frequencies of the antiresonant reflecting hollow waveguide, and can be expressed as

$$f_r = \frac{mc}{2t\sqrt{n_2^2-n_1^2}}, \quad m = 1, 2, 3, \ldots \tag{4}$$

Taking m = 2, 3, 4, and 5 into Eq. (4), resonant frequencies are obtained to be 306, 459, 612, and 765 GHz, respectively. At the resonant frequencies, the waveguide suffers the maximum loss.

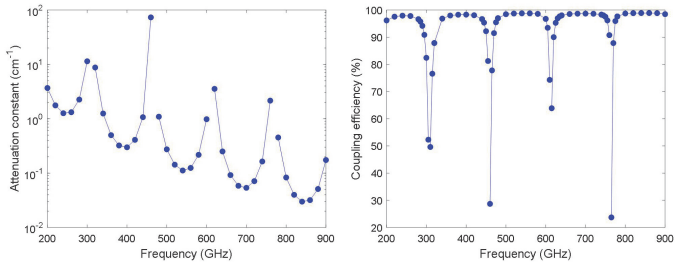

(a) (b)

Fig. 3 (a) Attenuation constant and (b) coupling efficiency of the slab-type antiresonant reflecting hollow waveguide as a function of frequency.

Assuming the beam waist of the input Gaussian beam is 5 mm, coupling efficiency of the slab-type antiresonant reflecting hollow waveguide can be calculated by referring to Eq. (2). The coupling efficiency is shown in Fig. 3(b) and regarded as a function of frequency. It is clear that at most frequencies the coupling efficiency is above 95%, indicating that the antiresonant reflecting hollow waveguide is excellent in coupling the THz power from the source to the waveguide. However, it is also observed that there are some dips existing in the figure, meaning that the coupling efficiency is relatively low at the corresponding fre-

quencies. Further examination shows that the frequencies at which low coupling efficiency takes place are 306, 459, 612, and 765 GHz, and these frequencies are exactly the resonant frequencies of the antiresonant reflecting hollow waveguide. Hence, to use the antiresonant reflecting hollow waveguide for THz wave transmission, it is important to choose the operating frequency, and the resonant frequencies should be avoided.

Now, we would like to investigate why the coupling efficiency is especially low at the resonant frequencies. Since the coupling efficiency is calculated by the electric field overlap integral of light source and the waveguide mode, we examine the electric field distributions of the input Gaussian source and the fundamental waveguide mode obtained at various frequencies. The results are normalized and shown in Fig. 4, where the field distribution of the fundamental mode of the antiresonant reflecting hollow waveguide is obtained with the frequencies locating in the pass-band of m = 5, *i.e.*, the forth pass-band in Fig. 3(a), which starts from 615 GHz to 760 GHz. Note that, in Fig. 4, the two vertical lines represent the boundaries of the cladding layer. It is obvious in Fig. 4 that field distributions at 615 and 760 GHz, which are close to the resonant frequencies of 612 and 765 GHz, are much different from the distribution of the Gaussian light source. In other words, serious mode mismatch occurs near the resonant frequencies, and this is the cause of the low coupling efficiency. Oppositely, field distributions at 660, 700, and 740 GHz are similar to the Gaussian profile, so that the coupling efficiency is high at these non-resonant frequencies, especially at the antiresonant frequencies.

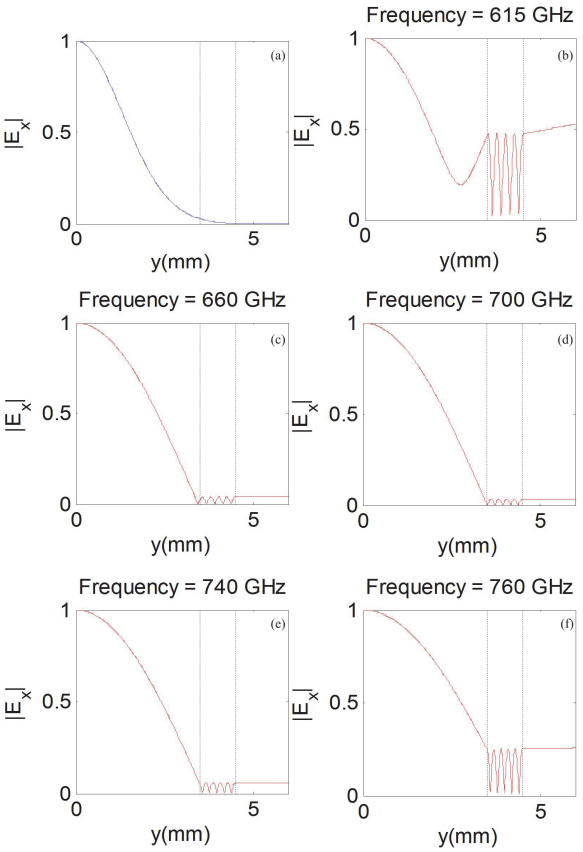

Fig. 4 Electric field distributions. (a) Input Gaussian beam. (b)-(f) Fundamental mode of slab-type antiresonant reflecting hollow waveguide obtained at 615, 660, 700, 740, and 760 GHz, respectively.

After discussing the coupling efficiency of the slab-type antiresonant reflecting hollow waveguide, we now continue to examine the behavior of the 2D version, *i.e.*, the THz pipe waveguide. Figure 5(a) plots the attenuation spectrum of the pipe waveguide. Clearly, there are several periodic pass-bands, similar to what appears for the case of the slab-type hollow waveguide as described in Fig. 3(a). Moreover, the calculated coupling efficiency, as shown in Fig. 5(b), also exhibits some dips at the resonant frequencies. Again, this can be attributed to the mode mismatch between the input Gaussian beam and the fundamental mode of the pipe waveguide. Note that, out of resonant frequencies, the coupling efficiency is about 80 ~ 90%, slightly lower than that of the slab-type antiresonant reflecting hollow waveguides.

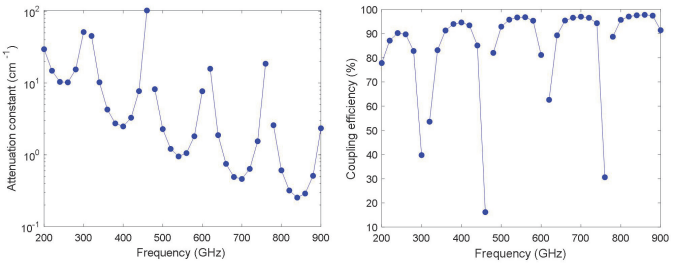

Fig. 5 (a) Attenuation constant and (b) coupling efficiency of the pipe waveguide as a function of frequency.

In order to better check the influence of resonant frequency on the coupling efficiency, we should now examine the situation where a pipe waveguide is directly connected to another pipe waveguide of different size. Here, we assume that the two connected pipe waveguides are with the same core width but different cladding layer thicknesses. For simulation, we assume the core width is w = 8 mm. We first consider the case in that a pipe waveguide of cladding thickness t = 1 mm is connected with another one of t = 0.5 mm. Figure 6(a) shows the attenuation spectra of the two pipe waveguides. Note that since the cladding layer thicknesses of the two pipe waveguides are different, according to Eq. (4), the resonant frequencies of the two waveguides are thus different. As shown in Fig. 6(a), the resonant frequencies are 306, 459, and 612 GHz for the pipe waveguide of t = 1 mm, while 306 and 612 GHz for the one of t = 0.5 mm. The coupling efficiency between the two pipe waveguides, *i.e.*, the percentage of power coupled from one pipe waveguide to another pipe waveguide, is shown in Fig. 6(b) as a function of frequency. It is found that, the coupling efficiency indeed finds dips at the three resonant frequencies.

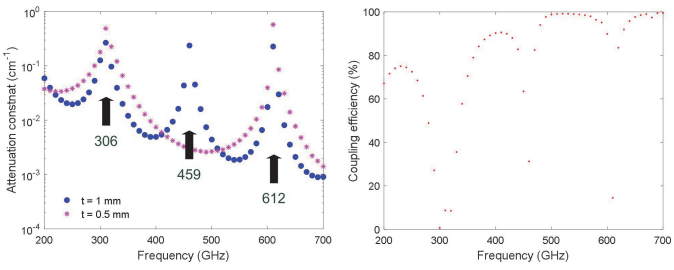

Fig. 6 (a) Attenuation spectra of pipe waveguides with cladding thicknesses of t = 1 mm and 0.5 mm. (b) Coupling efficiency between the two pipe waveguides as a function of frequency.

We have also considered another case where the pipe waveguide of cladding thickness t = 1 mm is connected with another one of t = 2 mm. Attenuation spectra of the two waveguides are shown in Fig. 7(a). Resonant frequencies for the pipe waveguide of t =1 mm are 306, 459, and 612 GHz, as aforementioned, and they are 230, 306, 382, 459, 536, 612, and 689 GHz for the one of t = 2 mm. The coupling efficiency between the two pipe waveguides is presented in Fig. 7(b). Again, coupling efficiency dips are clearly observed at the seven resonant frequencies.

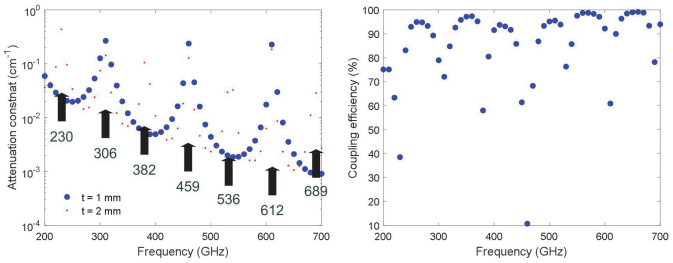

(a) (b)

Fig. 7 (a) Attenuation spectra of pipe waveguides with cladding thicknesses of t = 1 mm and 2 mm. (b) Coupling efficiency between the two pipe waveguides as a function of frequency.

4. CONCLUSION

We have numerically investigated the coupling efficiency for the 1D slab-type THz antiresonant reflecting hollow waveguides and the 2D hollow THz pipe waveguides. By assuming that the field pattern of the THz source is Gaussian, numerical results indicate that high coupling efficiency above 90% could be obtained at most of the frequencies. That is to say, the power emitted from the THz source could be coupled into the pipe waveguide effectively. This phenomenon is essential and could facilitate the development of THz technologies and applications. However, it is found that coupling efficiency is relatively low at resonant frequencies. Therefore, it is of high importance to choose the operating frequency carefully, and the resonant frequencies should be avoided for operation. We have also discussed the case where a pipe waveguide is connected to another pipe waveguide, with the same core width but different cladding layer thicknesses. This scenario is considered important for system integration. Simulation results suggest that, coupling efficiency between the connected pipe waveguides could be high, but again the resonant frequencies should be avoided.

REFERENCES

Arrand, H. F., Benson, T. M., Loni, A., Krueger, M. G., Thoenissen, M., and Lueth, H. (1997). "Self-aligned porous silicon optical waveguides." *Electron. Lett.*, **33**, 1724-1725.

Chou Chau, C.-T., Chou Chao Y.-F., Huang, H.J., Kumara, N.T.R.N., Kooh, M.R.R., Lim, C.M., and Chiang, H.-P. (2020). "Highly sensitive and tunable plasmonic sensor based on a nanoring resonator with silver nanorods." *Nanomaterials*, **10**, 1399.

Chou Chau, Y.-F., Chen, K.-H., Chiang, H.-P., Lim, C.M., Huang, H.J., Lai, C.-H., and Kumara, N.T.R.N. (2019a). "Fabrication and characterization of a metallic–dielectric nanorod array by nanosphere lithography for plasmonic sensing application." *Nanomaterials*, **9**, 1691.

Chou Chau, Y.-F., Chou Chao, C.-T., Huang, H.J., Kumara, N.T.R.N., Lim, C.M., and Chiang, H.-P. (2019b). "Ultra-high refractive index sensing structure based on a metal-insulator-metal waveguide-coupled T-shape cavity with metal nanorod defects." *Nanomaterials*, **9**, 1433.

Duguay, M.A., Kukubun, Y., Koch, T.L., and Pfeiffer, L. (1986). "Antiresonant reflecting optical waveguides in SiO_2-Si multilayer structures." *Appl. Phys. Lett.*, **49**, 13-15.

Dupuis, A., Allard, J.F., Morris, D., Stoeffler, K., Dubois, C., and Skorobogatiy, M. (2009). "Fabrication and THz loss measurements of porous subwavelength fibers using a directional coupler method." *Opt. Express*, **17**, 8012-8028.

Han, Z., Forsberg, E., and He, S. He (2007). "Surface plasmon Bragg gratings formed in metal–insulator–metal waveguides." *IEEE Photon. Technol. Lett.*, **19**, 91-93.

Lai, C.-H., Hsueh, Y.-C., Chen, H.-W., Huang, Y.-J., Chang, H.-C., and Sun, C.-K. (2009). "Low-index terahertz pipe waveguides." *Opt. Lett.*, **34**, 3457-3459.

Lai, C.-H., You, B., Lu, J.-Y., Liu, T.-A., Peng, J.-L., Sun, C.-K., and Chang, H.-C. (2010). "Modal characteristics of antiresonant reflecting pipe waveguides for terahertz waveguiding." *Opt. Express*, **18**, 309-322.

Lai, C.-H., J.-Y., Liu, and Chang, H.-C. (2011). "Adding metallic layers outside terahertz antiresonant reflecting waveguides: the influence on loss spectra." *J. Opt. Soc. Am. B*, **28**, 2200-2206.

Matsui, T., Nakajima, K., and Fukai, C. (2009). "Applicability of photonic crystal fiber with uniform air-hole structure to high-speed and wideband transmission over conventional telecommunication bands." *J. Lightw. Technol.*, **27**, 5410-5416.

Milvich, J., Kohler, D., Freude, W., and Koos, C. (2018). "Surface sensing with integrated optical waveguides: a design guideline." *Opt. Express*, **26**, 19885-19906.

Schultz, P.C. (1979). "Progress in optical waveguide process and materials." *Appl. Opt.*, **18**, 3684-3693.

Wang, J. and Dong, J. (2020). "Optical waveguides and integrated optical devices for medical diagnosis, health monitoring and light therapies." *Sensors*, **20**, 3981.

Yang, H., Castaneda, J.A., and Alexopoulos, N.G. (1990). "An integral equation analysis of an infinite array of rectangular dielectric waveguides." *IEEE Trans. Microwaves Theory Tech.*, **38**, 873-880.

Yee, K. S. (1966). "Numerical solution of initial boundary value problems involving maxwells equation in isotropic media." *IEEE Trans. Antennas Propag.*, **14**, 302-307.

Yu, C.-P. and Chang, H.-C. (2004). "Yee-mesh-based finite difference eigenmode solver with PML absorbing boundary conditions for optical waveguides and photonic crystal fibers." *Opt. Express*, **12**, 6165-6177.